Global variability of optical backscattering by non-algal particles from a Biogeochemical-Argo dataset

Marco Bellacicco, Marin Cornec, E. Organelli, R. J W Brewin, G. Neukermans, G. Volpe, Marie Barbieux, A. Poteau, C. Schmechtig, F. d'Ortenzio, et al.

Bellacicco Marco (Orcid ID: 0000-0002-0477-173X)
Organelli Emanuele (Orcid ID: 0000-0001-8191-8179)
Neukermans Griet (Orcid ID: 0000-0002-8258-3590)
Volpe Gianluca (Orcid ID: 0000-0002-3916-5393)
Poteau Antoine P (Orcid ID: 0000-0002-0519-5180)
Schmechtig Catherine (Orcid ID: 0000-0002-1230-164X)
D'Ortenzio Fabrizio (Orcid ID: 0000-0003-0617-7336)
Marullo Salvatore (Orcid ID: 0000-0003-4203-0956)
Claustre Hervé (Orcid ID: 0000-0001-6243-0258)
Pitarch Jaime (Orcid ID: 0000-0003-0239-0033)

Global variability of optical backscattering by non-algal particles from a Biogeochemical-Argo dataset

M. Bellacicco[1,2], M. Cornec[2], E. Organelli[2], R.J.W. Brewin[3,4], G. Neukermans[2], G. Volpe[5], M. Barbieux[2], A. Poteau[2], C. Schmechtig[2], F. D'Ortenzio[2], S. Marullo[1], H. Claustre[2] and J. Pitarch[6]

[1]Italian National Agency for New Technologies, Energy and Sustainable Economic Development (ENEA), Via E. Fermi 45, 00044, Frascati, Italy.
[2]Sorbonne Université, CNRS, Laboratoire d'Océanographie de Villefranche, LOV, F-06230 Villefranche-sur-Mer, France.
[3]Centre for Geography and Environmental Science, University of Exeter, Penryn Campus, Cornwall, TR10 9FE, UK
[4]Plymouth Marine Laboratory, Prospect Place, The Hoe, Plymouth PL1 3DH, UK.
[5]Institute of Marine Sciences (ISMAR)-CNR, Via Fosso del Cavaliere, 100, 00133, Rome, Italy.
[6]NIOZ Royal Netherlands Institute for Sea Research, Department of Coastal Systems, and Utrecht University, Den Burg, Texel, the Netherlands.

*Corresponding author mail-address: marco.bellacicco@enea.it

Abstract

Understanding spatial and temporal dynamics of non-algal particles (NAP) in open ocean is of the utmost importance to improve estimations of carbon export and sequestration. These particles covary with phytoplankton abundance but also accumulate independently of algal dynamics. The latter likely represents an important fraction of organic carbon but it is largely overlooked. A possible way to study these particles is *via* their optical backscattering properties (b_{bp}) and relationship with chlorophyll-*a* (Chl). To this aim, we estimate the fraction of b_{bp} associated with the NAP portion (b_{bp}^k) that does not covary with Chl by using a global Biogeochemical-Argo dataset. We quantify the spatial, temporal and vertical variability of b_{bp}^k. In the northern productive areas, b_{bp}^k is a small fraction of b_{bp} and shows a clear seasonal cycle. In the Southern Ocean, b_{bp}^k is a major fraction of total b_{bp}. In oligotrophic areas, b_{bp}^k has a smooth annual cycle.

Keywords: non-algal particles, optical backscattering, global ocean, BGC-Argo floats

1. Introduction

In the ocean, the pool of non-algal particles (NAP) includes: i) heterotrophic organisms such as bacteria, micro-grazers and viruses, ii) organic particles of detrital origin such as faecal pellets and cell debris, iii) mineral particles of both biogenic (*e.g.* calcite liths and shells) and terrestrial origin (*e.g.* clays and sand), iv) bubbles (Sosik et al., 2008) and v) plastics. Understanding of the spatial and temporal dynamics of NAP in the open ocean can improve estimations of carbon export and sequestration (Azam et al., 1983; Bishop and Wood, 2009). NAP can covary with phytoplankton abundance or accumulate regardless of algal dynamics. In such a context, a possible way to monitor these particles and distinguish between these two fractions is *via* their optical backscattering properties and relationship with chlorophyll-*a*. Unfortunately, only a few studies have concerned the backscattering properties of NAP up to date (b_bNAP; units of m^{-1}) (Cho and Azam, 1990; Morel and Ahn, 1990, 1991; Stramski and Kiefer, 1991), as a consequence of the difficulties in directly measuring this optical coefficient. Indeed, optical backscattering sensors measure backscattering of all particles suspended in seawater (b_{bp}; units of m^{-1}) (Dall'Olmo et al., 2009, 2012, Westberry et al., 2010), which includes algal particles among the others. The NAP signal cannot be separated from that of phytoplankton. However, total b_{bp} offer the great advantage to be measured by satellite and *in situ* from Biogeochemical-Argo (aka BGC-Argo) floats. Using b_{bp} we can thus observe the global ocean with high spatial and temporal resolutions.

The first attempt to derive b_bNAP in the open waters was by Behrenfeld et al. (2005) (hereafter Be05) using five-years of ocean colour remote sensing data. They computed the fraction of the b_{bp} that does not covary with phytoplankton chlorophyll-*a* concentration (Chl; units of mg m^{-3}), and estimated it as the offset of a linear regression between satellite-derived b_{bp} and Chl when Chl concentrations were > 0.14 mg m^{-3}. This offset was defined as the *background* of the b_bNAP (hereafter b_{bp}^k; units of m^{-1}) and refers only to a fraction of the total b_{bp} signal caused by NAP that thus does not covary with Chl (*i.e.* phytoplankton).

In Be05, b_{bp}^k is assumed to be a constant value both in space and time (*i.e.* 3.5·10^{-4} m^{-1}). Be05 attributed it to "*a stable heterotrophic and detrital component of the surface particle population and therefore independent of the phytoplankton dynamics*". Recently, Bellacicco et al. (2016) (hereafter Blc16) applied Be05's approach for distinct bioregions and seasons in the Mediterranean Sea, and showed that b_{bp}^k has instead a marked regional and seasonal variability. Such a result thus confirmed that the heterotrophic and detrital components at the sea surface are neither negligible nor stable, but highly variable in seawater (Siokou-Frangou et al., 2010). These observations were consistent with field observations of Chl and b_{bp} from the BOUSSOLE buoy in which the Chl-b_{bp} relationship was highly dependent on the season of the area (Antoine et al., 2011). The variability of the b_{bp}^k by Blc16 was also later confirmed by Bellacicco et al., (2018) for the global ocean (hereafter Blc18). Indeed, Blc18 highlighted two distinct oceanic areas: the productive sub-polar North Atlantic Ocean, where b_{bp}^k and particle biomass (*i.e.* phytoplankton cells) are anti-correlated; and the Southern Ocean, where b_{bp}^k signal is mainly driven by inorganic particles, such as algal coccoliths (Balch et al., 2016, 2018), bubbles or foam that occur in the stormy seas (Stramski et al.,

2004). However, ocean-colour data used in these works are only sensitive to the surface layer. The increasing number of BGC-Argo floats, equipped with b_{bp} sensors, can therefore expand the analysis to underlying layers.

The relationship between b_{bp} and Chl is also influenced by phytoplankton specific composition and diversity (*e.g.* size, shape, internal structure), physiology (*e.g.,* photoacclimation) and the nature of NAP itself (Stramski et al., 2004; Dall'Olmo et al., 2009, 2012). Therefore, an analytical fit between b_{bp} and Chl that includes these factors may improve b_{bp}^k estimations. In such a context, Brewin et al., (2012) (hereafter Br12) presented a relationship between b_{bp} and Chl that accounted for modifications in phytoplankton size. The model, based on surface *in situ* observations, included separated b_{bp} terms for small and large cells that dominated the overall fit at different Chl ranges. This model also estimated b_{bp}^k, as the *offset* of the fit between b_{bp} and Chl in clear waters where this relationship converged to a flat value for low Chl values. The b_{bp}^k parameter was interpreted as a constant *background* of NAP (*e.g.* heterotrophic bacteria, detritus, viruses, minerogenic particles), possibly partly influenced by very small phytoplankton (*e.g.* prochlorophytes).

In this study, the Br12 model is applied to an extensive global dataset of Chlorophyll-*a* fluorescence, here converted in Chl, and b_{bp} (700) measurements acquired from BGC-Argo profiling floats. In detail, we estimate b_{bp}^k across different oceanic areas (*i.e.* from productive to ultra-oligotrophic zones), months, and in two distinct layers of the water column: at the surface and within the euphotic layer. To interpret our estimations of b_{bp}^k, we use as a reference of the b_{bp}^k value in each region the median b_{bp} at $950 - 1000$ meters also derived from BGC-Argo observations. At these depths b_{bp} is entirely due to the fraction of NAP that does not covary with Chl (Poteau et al., 2017).

2. Data and Methods

2.1 The BGC-Argo dataset

An array of 425 BGC-Argo profiling floats was deployed around the World's oceans as part of several national and international programs (http://biogeochemical-argo.org), and collected data from 30/05/10 to 31/12/18 every one up to ten days. These floats acquired 0-1000 m vertical profiles of pressure, temperature and salinity by a Seabird Scientific SBE 41 Conductivity-Temperature-Depth (CTD) sensor, Chlorophyll-*a* fluorescence (FChl*a*; excitation at 470 nm, emission at 695 nm) and the angular scattering function at 700 nm by Seabird-WetLABS combo sensors (mostly FLBB, ECOTRIPLET, or MCOMS). Chlorophyll-*a* fluorescence is then converted to Chl concentration (units of mg m^{-3}) and the angular scattering to particulate optical backscattering coefficient b_{bp} (units of m^{-1}) (see supplementary materials). All the data were downloaded from the Coriolis database (ftp://ftp.ifremer.fr/ifremer/argo/dac/coriolis) and quality controlled (see supplementary material). The BGC-Argo floats (more than 35000 correspondent Chl and b_{bp} data) over global ocean used in the present study are partitioned into 18 areas (Figure 1). The dataset of Chl and b_{bp} here used, represents the update version of the databases BOPAD-prof and BOPAD-surf by Organelli et al. (2017). The depth of euphotic zone, Z_{eu} (units of m), which

is the depth where PAR reaches 1% of its surface value, was estimated from the Chl profile through the iterative process described in Morel and Maritorena (2001). Subsequently, the first optical depth, Z_{pd} (units of m), was calculated as $Z_{eu}/4.6$ (Morel, 1988). Finally, for each profile, the mean and standard deviation of Chl and b_{bp} were calculated within: i) the surface layer: the layer between sea surface and the first optical depth; ii) the euphotic layer: the layer between sea surface and euphotic zone; and iii) the bottom layer: the layer between 950 and 1000 m.

2.2 b_{bp}^k estimation: the model

In this study, the model developed by Brewin et al., (2012) is used to compute b_{bp}^k. The b_{bp} is modeled as a function of Chl and takes into account the fractional contributions of small and large phytoplankton, as follows:

$$b_{bp} = C_1^m \cdot \left[b_{bp,1}^* - b_{bp,2}^*\right]\left[1 - e^{-S_1 \cdot \text{Chl}}\right] + b_{bp,2}^* \cdot \text{Chl} + b_{bp}^k \qquad [1]$$

where the subscript 1 and 2 refer to two populations of phytoplankton cells partitioned according to size: 1 is for cells $< 20\mu m$ while 2 is for cells $> 20\mu m$; $b_{bp,1}^*$ and $b_{bp,2}^*$ refer to the Chl-specific b_{bp} coefficients associated with environments dominated by the two populations of phytoplankton; C_1^m and S_1 refer to the maximum Chl concentration population 1 can reach and the initial slope relating the Chl concentration of population 1 to total Chl, respectively. The term b_{bp}^k refers to the *background* b_{bp} coefficient. The general equation of the model can be simplified as:

$$b_{bp} = c \cdot \left[1 - e^{(-S_1 Chl)}\right] + b_{bp,2}^* \cdot \text{Chl} + b_{bp}^k, \qquad [2]$$

in which $b_{bp,2}^*$ is the slope, b_{bp}^k is the intercept of the fit, while $c = C_1^m\left[b_{bp,1}^* - b_{bp,2}^*\right]$ and S_1 terms are the coefficients of the non-linear part of the model. The $b_{bp,2}^*$, b_{bp}^k, c and S_1 coefficients are found from fitting Eq. 2 to b_{bp} and Chl data by using the iterative bi-square method (see paragraph 2.3). The initial guess for the four parameters are reported in Table S1. These values are in the range and order of magnitude of the values reported in Brewin et al., (2012). This model reduces to the Be05, Blc16 and Blc18 linear models if the non-linear term is discarded out, which would be the case where $b_{bp,1}^*$ and $b_{bp,2}^*$ tend to the same value. This model represents an evolution of the previous published model (*i.e.* Be05, Blc16 and Blc18) because of it takes into account the phytoplankton populations variability in the Chl-b_{bp} relationship and thus for b_{bp}^k estimations. In addition, the inclusion of the non-linear term introduces more flexibility reducing the fit errors for the areas here analyzed (see Figures S1 and S2).

The Eq. 2 is applied to each area (spatially-resolved with the temporal aggregation approach reported in Figure 1), and for every month (spatially- and temporal-resolved approach) for the two layers.

The ratio between the b_{bp}^k value found in the surface and in the bottom layers, and analogously for the euphotic layer, enables understanding the difference between upper and deeper layers for each area of interest. It is computed as:

$$\widehat{b_{bp}^k} = \frac{b_{bp,surface}^k}{b_{bp,bottom}^k} \qquad \qquad [3a]$$

$$\widehat{b_{bp}^k} = \frac{b_{bp,euphotic}^k}{b_{bp,bottom}^k} \qquad \qquad [3b]$$

In addition to this ratio, $\overline{b_{bp}^k}$ is here defined as the fraction of the b_{bp}^k with respect to the median b_{bp} (in %) giving an understanding on the relationship between NAP and particle biomass in the different areas, and the layers, of the ocean:

$$\overline{b_{bp}^k} = \frac{b_{bp}^k}{b_{bp}} \qquad \qquad [4]$$

2.3 Model fit and statistics

For all the computations, Chl measurements below the value of 0.01 mg m^{-3} are considered too noisy for a proper estimation of b_{bp}^k and are filtered out from the dataset. The model in Eq. 2 is fitted to the data using the iterative bi-square method which minimizes a weighted sum of squared errors, where the weight given to each data point decreases with the distance from the fitted curve (Huber, 1981). Therefore, the error function is sensitive to the bulk of the data and the effect of outliers is thus reduced. This error function is minimized through the Trust-Region algorithm (Moré and Sorensen, 1983) and the final fit estimate is found after a maximum of 400 iterations. For each b_{bp}^k the 95% confidence intervals and two-standard deviation as confidence limit ($\pm 2\sigma$) are computed. In order to assess the model performance for the b_{bp}^k calculation, the root mean square (RMS; in m^{-1}) error between the modeled-b_{bp} and measured-b_{bp} are computed. The RMS is calculated according to:

$$RMS = \sqrt{\frac{1}{N} \sum_{i=1}^N \left(b_{bp,modeled,i} - b_{bp,measured,i} \right)^2}$$

3. Results and Discussion

3.1 Global overview of b_{bp}^k

Aggregated quality-controlled data within the surface layer for all areas and months (N=36067) are shown in Figure 2a. The b_{bp} coefficients increase with Chl but with relatively

constant b_{bp} for low Chl values (Figure 2a). This behavior is consistent with previous observations by Behrenfeld et al. (2005) and Brewin et al. (2012), and is considered to be the consequence of two distinct oceanic conditions: "*photoacclimation-dominance*" and "*biomass-dominance*" of Chl signal. The former is typical of oligotrophic areas (*e.g.* subtropical gyres) where variability of Chl is uncoupled with biomass and the process of acclimation to light and nutrients drives Chl variations (Siegel et al., 2013; Halsey and Jones, 2015; Barbieux et al., 2018). On the reverse, the latter case is typical of most productive areas where Chl and b_{bp} strongly covary (Dall'Olmo et al., 2009, 2012; Westberry et al., 2010). The high Chl-b_{bp} co-variability is a clear indication that particles (and biomass) covary with phytoplankton abundance, while the physiological photoacclimation process playing a secondary role in determining the Chl variations.

Here, the application of the Br12 model to these BGC-Argo data leads to a b_{bp}^{k} equal to $5.0 \cdot 10^{-4}$ m^{-1} at the surface, a value higher than that found by Be05 ($3.5 \cdot 10^{-4}$ m^{-1} at 443 nm). On the other hand, Br12 reported $7.0 \cdot 10^{-4}$ m^{-1} for 470 nm and $5.6 \cdot 10^{-4}$ m^{-1} at 526 nm. Blc18 found a median b_{bp}^{k} value equal to $9.5 \cdot 10^{-4}$ m^{-1} based on 19-years of ocean colour data. These values are comparable as the spectral variability is limited in case of b_{bp} (±30% between 443nm and 700nm when assuming b_{bp} decreasing as a power law with slope equal to 0.7). In relative terms, our study shows that b_{bp}^{k} dominate within the surface layer as it accounts for ±57% of the total b_{bp} measured by all BGC-Argo floats, a remarkably high percentage.

An increased Chl-b_{bp} co-variability is observed within the euphotic layer (Figure 2b; *N*=37322). The derived b_{bp}^{k} is not comparable to our estimates from the surface layer or from previous satellite observations because it includes deeper layers where there is high particle concentration, as for example oligotrophic areas such as the subtropical gyres and the eastern Mediterranean Sea (Volpe et al., 2007; Barbieux et al., 2018). The first estimation of b_{bp}^{k} for this layer is a value of $3.9 \cdot 10^{-4}$ m^{-1}, and accounts for ±45% of the total b_{bp}, suggesting that in the euphotic layer NAP are more correlated to Chl than at the surface.

3.2 Geographical distribution of b_{bp}^{k}

Figure 3a shows b_{bp}^{k} estimations for the surface, euphotic and bottom layers within each geographical area sampled by BGC-Argo floats. In surface layer, the range of variability spans between 10^{-4} m^{-1} and 10^{-3} m^{-1}, consistent with global ocean-colour estimations (Bellacicco et al., 2018). Lower variability characterizes the euphotic layer (of a factor of ~6), from ~$1.0 \cdot 10^{-4}$ m^{-1} to $6.0 \cdot 10^{-4}$ m^{-1}. For the bottom layer, variability is the lowest, between $2.0 \cdot 10^{-4}$ m^{-1} and $4.0 \cdot 10^{-4}$ m^{-1}. The two upper layers display a latitudinal gradient, with a general b_{bp}^{k} decrease from northern to southern oceans. b_{bp}^{k} in the bottom layer does not show a clear geographical pattern and remains relatively constant across all sampled oceanic areas.

Figure 3b shows the $\widehat{b_{bp}^{k}}$ for each area, the ratios between the spatially-resolved b_{bp}^{k} found at the surface and euphotic layers with the estimation for the bottom layer. Globally, $\widehat{b_{bp}^{k}}$ is higher in the upper layer than the at the bottom from mid- to low-latitudes, while b_{bp}^{k} at the bottom is higher than at the surface in most productive seas such as the NASPG, SAZ, PFZ and ASZ_SIZ areas (Uitz et al., 2009; Alkire et al., 2014; Artega et al., 2018). In these

areas, $\overline{b_{bp}^k}$ is only a small fraction of the total b_{bp} in surface waters ($< 20\%$; Figure 3c) as a consequence of the higher relative variability in the b_{bp} and phytoplankton abundance (Alkire et al., 2014). In the NASPG, characterized by high phytoplankton biomass, $\overline{b_{bp}^k}$ is lower than 10%. It means that b_{bp} is more dominated by particles that covary with phytoplankton cells (see Eq. 1), thus being more influenced by phytoplankton dynamics.

In the Southern Ocean (*i.e.* STZ, SAZ, PFZ and ASZ_SIZ areas), $\overline{b_{bp}^k}$ ranges from 15% (*i.e.* PFZ) to 60% (*i.e.* STZ) for surface waters suggesting inorganic particles (*e.g.* coccoliths) can also drive the b_{bp}^k signal (Figure 3c). Indeed, coccoliths concentrations covary with b_{bp} because they scatter light with high efficiency (Balch et al. 2016; 2018). The b_{bp}^k values, and their order of magnitude, are consistent with measurements of b_{bp} from $CaCO_3$ reported in Balch et al. (2016) along the Great Calcite Belt (GCB) (their Figure 2c). Thus, in these areas of the Southern Ocean, the b_{bp}^k may be related to the coccolithophorids seasonality (*i.e.* skeleton compounds of no longer living cells; b_{bp}^k is the b_{bp} when Chl is zero) (Balch et al. 2016; 2018; Bellacicco et al., 2018).

In less productive areas (*e.g.* EMS, IEQ, NASTG, SISTG, SASTG, SPSTG; Figure 3d), $\overline{b_{bp}^k}$ is greater than 80% at the surface layer, consistent with previous findings (Brewin et al., 2012; Bellacicco et al., 2018). These areas are characterized by limited nutrients availability determining low phytoplankton biomass, especially pico- and nano-phytoplankton dominated communities (Bricaud et al., 2004; Mignot et al., 2014), which are rapidly recycled in the surface layer thus supporting relatively high bacterial and detrital biomass. For the euphotic layer, much of the b_{bp} can be related to phytoplankton biomass as highlighted by a lower $\overline{b_{bp}^k}$ value of around 60%. This is the consequence of the subsurface chlorophyll maximum (SCM) which is deeper in the subtropical gyres and oligotrophic seas as found by Mignot et al., (2014) and Barbieux et al., (2019). It determines that, at depth, there is an increase of phytoplankton biomass and of NAP covarying with phytoplankton: the b_{bp}^k coefficient indeed decreases from the surface to the euphotic layers (Figure 3a).

3.3 Seasonal variability of b_{bp}^k

The b_{bp}^k values within surface and euphotic layers show a clear seasonal cycle with maxima during the productive periods ($b_{bp}^k > 5.0 \cdot 10^{-4}$) and minima during the low productive periods ($b_{bp}^k < 4.0 \cdot 10^{-4}$) in all the areas outside the oligotrophic seas (*e.g.* NS, NASPG, WMS, EMS, STZ, SAZ, PFZ, ASZ_SIZ) (Figure 4).

In the NASPG, b_{bp}^k shows high values during the well-known spring bloom and low values from December to April (Briggs et al., 2011; Alkire et al., 2014; Mignot et al., 2018). In the Southern Ocean, and especially SAZ, PFZ and ASZ_SIZ areas, b_{bp}^k shows the maxima values from December to April (*i.e.* period of bloom) while the minima are detected in the period May-September.

In the Mediterranean Sea (*i.e.* WMS and EMS), the seasonal cycle varies within the sub-basins showing different amplitude and shape, clearly linked to the regional trophic

regimes. WMS shows b_{bp}^k values higher than the eastern ones confirming the presence of a general decreasing eastward gradient for this coefficient. In the western basin of Mediterranean Sea, deep-water formation dynamics and/or the generally shallow nutricline results in a maximum value in April. On the contrary, maxima generally occur earlier between February and March in the eastern Mediterranean basin. These results confirm Bellacicco et al., (2016) findings for this semi-enclosed basin. In their work, b_{bp}^k was demonstrated to be variable both in space and time with a marked seasonality in the different bio-regions of both the sub-basins. As shown by Bellacicco et al., (2016), periods characterized by lower b_{bp}^k (*e.g.* summer) are also associated with higher variability and uncertainties in the estimations. This is valid for the b_{bp}^k both in the surface and euphotic layers, and has to be taken into account in the interpretation of these results (see Tables S3 and S4).

The b_{bp}^k at the bottom layer shows a smoother seasonal cycle in respect to what occur in the upper layers. As found by Poteau et al., (2017), an annual cycle is only observed at the Southern Ocean and sub-polar North Atlantic area, regions with the largest amplitude in the seasonal cycles at the surface and euphotic layer (Figure 4) due to blooms of large phytoplankton (Alkire et al., 2014; Barbieux et al., 2018). Poteau et al., (2017), indeed, suggested that the b_{bp}^k at the depth can be mostly related to disaggregation of these large settling particles.

The seasonal cycle of b_{bp}^k in the less productive seas for all the layers is low, suggesting low NAP seasonal variations (*e.g.* detrital matter, heterotrophic bacteria, virus). The b_{bp}^k estimation for each month appears to be nearly constant throughout the year (Figure 4) and thus b_{bp} may be controlled mostly by b_{bp}^k, as highlighted also in Figure 3c.

4. Conclusions

In this work, an extensive global dataset of Chl and b_{bp} (700) measurements acquired from Biogeochemical-Argo (BGC-Argo) profiling floats was analyzed. Specifically, we investigated and describe the spatial, vertical and temporal variability of b_{bp}^k at global scale. The main results are:

o b_{bp}^k shows a similar order of magnitude in both surface and euphotic layers, as previously published works based on ocean-colour data: ranging between 10^{-4} and 10^{-3} m^{-1}.

o   In the surface layer, the b_{bp}^k increase from southern to the northern hemisphere, confirming what was found by Bellacicco et al., (2018) using ocean-colour data.

o   In the surface layer of most productive areas (*e.g.* NASPG), the b_{bp}^k is only a small fraction of the total b_{bp} (< 20%), while in the oligotrophic waters, b_{bp}^k is the main contributor to the total b_{bp} (> 80%). In the euphotic layer of the oligotrophic areas, the b_{bp}^k has a lower contribution to the total b_{bp} (average value of 65%).

o In the surface and euphotic layers, the b_{bp}^k shows strong seasonal variability in the main productive areas of the global ocean, such as NASPG and the Southern Ocean areas. b_{bp}^k has instead a weak temporal variability in the low productivity areas, such as the subtropical gyres. This is valid also for the b_{bp}^k estimations at the bottom layer.

The b_{bp}^k is a key parameter for satellite estimations of phytoplankton biomass in terms of carbon (Behrenfeld et al., 2005, 2016; Bellacicco et al., 2016, 2018, 2019; Martinez-Vicente et al., 2017; Westberry et al., 2008, 2016). Recently, Bellacicco et al., (2018) highlighted the difference (of around a factor of 2) in the phytoplankton carbon biomass estimation from space by using a b_{bp}^k variable in space, rather than a single value. Consequently, inclusion of this reported spatial-temporal and depth variations of b_{bp}^k into phytoplankton carbon models may help to improve their predictions from remote sensing data (Martinez-Vicente et al., 2017) but also from BGC-Argo floats (Mignot et al., 2014, 2018).

Remote optical-based predictions and interpretation of phytoplankton carbon models would also benefit from a better understanding of NAP composition and which particles generate the b_{bp} signal across the world's oceans. Indeed, submicron detrital particles have long been considered as the main source of b_{bp} (Stramski et al., 2004). However, Organelli et al. (2018) has highlighted that b_{bp} is mainly due to particles with diameters between 1-10 μm which may also include NAP and aggregates. This latter study thus opens the way to new questions on the sources of the open-ocean b_{bp} signal that are critical to improving our interpretation of open-ocean b_{bp}.

Future research challenges should therefore be directed to: (i) understand the drivers of the observed spatio-temporal variability and explore the composition of NAP across the world's oceans and how it influences the b_{bp} and b_{bp}^k signal; (ii) study the impact on biogeochemistry of b_{bp}^k, *e.g.* on the particles assemblage in different ocean trophic regimes (*i.e.* subpolar, subtropical); (iii) include b_{bp}^k spatial and temporal variability into phytoplankton carbon estimations from space and its connections with phytoplankton physiology; and most importantly (iv): advance technology for (autonomous) optical measurements of NAP directly, for example by exploiting the birefringence properties of mineral particles such as calcite compounds (Guay and Bishop, 2002; Bishop and Wood, 2009), and acquire spectral angular scattering to better understand the influence of bubbles and plastics (Zhang et al., 1998; Twardowski et al., 2012).

Acknowledgements

References

1. Alkire, M. B., Lee, C., D'Asaro, E., Perry, M. J., Briggs, N., Cetinić, I., & Gray, A. (2014). Net community production and export from Seaglider measurements in the North Atlantic after the spring bloom. *Journal of Geophysical Research: Oceans*, 119, 6121–6139. https://doi.org/10.1002/2014JC010105

2. Antoine, D., Siegel, D. A., Kostadinov, T., Maritorena, S., Nelson, N. B., Gentili, B., ... & Guillocheau, N. (2011). Variability in optical particle backscattering in contrasting bio-optical oceanic regimes. *Limnology and Oceanography*, *56*(3), 955-973.

3. Arteaga, L., Haëntjens, N., Boss, E., Johnson, K. S., & Sarmiento, J. L. (2018). Assessment of export efficiency equations in the Southern Ocean applied to satellite-based net primary production. *Journal of Geophysical Research: Oceans*, *123*(4), 2945-2964

4. Azam, F., Fenchel, T., Field, J. G., Grey, J. S., Meyer-Reil, L. A., & Thingstad, F. (1983). The ecological role of water-column microbes. *Mar. ecol. Prog. ser*, *10*, 257-263.

5. Balch, W. M., Bates, N. R., Lam, P. J., Twining, B. S., Rosengard, S. Z., Bowler, B. C., ... & Rauschenberg, S. (2016). Factors regulating the Great Calcite Belt in the Southern Ocean and its biogeochemical significance. *Global Biogeochemical Cycles*, *30*(8), 1124-1144.

6. Balch, W. M. (2018). The ecology, biogeochemistry, and optical properties of coccolithophores. *Annual review of marine science*, *10*, 71-98.

7. Barbieux, M., Uitz, J., Bricaud, A., Organelli, E., Poteau, A., Schmechtig, C., ... & D'Ortenzio, F. (2018). Assessing the Variability in the Relationship Between the Particulate Backscattering Coefficient and the Chlorophyll a Concentration from a Global Biogeochemical-Argo Database. *Journal of Geophysical Research: Oceans*, *123*(2), 1229-1250.

8. Behrenfeld, M. J., Boss, E., Siegel, D. A., & Shea, D. M. (2005). Carbon-based ocean productivity and phytoplankton physiology from space. *Global biogeochemical cycles*, *19*(1).

9. Behrenfeld, M. J., O'Malley, R. T., Boss, E. S., Westberry, T. K., Graff, J. R., Halsey, K. H., ... & Brown, M. B. (2016). Revaluating ocean warming impacts on global phytoplankton. *Nature Climate Change*, *6*(3), 323.

10. Bellacicco, M., Volpe, G., Colella, S., Pitarch, J., & Santoleri, R. (2016). Influence of photoacclimation on the phytoplankton seasonal cycle in the Mediterranean Sea as seen by satellite. *Remote Sensing of Environment*, *184*, 595-604.

11. Bellacicco, M., Volpe, G., Briggs, N., Brando, V., Pitarch, J., Landolfi, A., ... & Santoleri, R. (2018). Global Distribution of Non-Algal Particles From Ocean Color Data and

Implications for Phytoplankton Biomass Detection. *Geophysical Research Letters*, *45*(15), 7672-7682.

12. Bellacicco, M., Vellucci, V., Scardi, M., Barbieux, M., Marullo, S., & D'Ortenzio, F. (2019). Quantifying the Impact of Linear Regression Model in Deriving Bio-Optical Relationships: The Implications on Ocean Carbon Estimations. *Sensors*, *19*(13), 3032.

13. Bishop, J. K., & Wood, T. J. (2009). Year-round observations of carbon biomass and flux variability in the Southern Ocean. *Global Biogeochemical Cycles*, *23*(2).

14. Brewin, R. J., Dall'Olmo, G., Sathyendranath, S., & Hardman-Mountford, N. J. (2012). Particle backscattering as a function of chlorophyll and phytoplankton size structure in the open-ocean. *Optics express*, *20*(16), 17632-17652.

15. Bricaud, A., Babin, M., Claustre, H., Ras, J., & Tièche, F. (2010). Light absorption properties and absorption budget of Southeast Pacific waters. *Journal of Geophysical Research*, 115, C08009. https://doi.org/10.1029/2009JC005517.

16. Briggs, N., Perry, M. J., Cetinić, I., Lee, C., D'Asaro, E., Gray, A. M., & Rehm, E. (2011). High-resolution observations of aggregate flux during a sub-polar North Atlantic spring bloom. *Deep Sea Research Part I: Oceanographic Research Papers*, *58*(10), 1031-1039.

17. Cho, B. C., & Azam, F. (1990). Biogeochemical significance of bacterial biomass in the ocean's euphotic zone. *Marine ecology progress series. Oldendorf*, *63*(2), 253-259

18. Dall'Olmo, G., Westberry, T. K., Behrenfeld, M. J., Boss, E., & Slade, W. H. (2009). Direct contribution of phytoplankton-sized particles to optical backscattering in the open ocean. *Biogeosciences Discussions*, *6*(1).

19. Dall'Olmo, G., Boss, E., Behrenfeld, M. J., & Westberry, T. K. (2012). Particulate optical scattering coefficients along an Atlantic Meridional Transect. *Optics express*, *20*(19), 21532-21551.

20. Gray, A. R., Johnson, K. S., Bushinsky, S. M., Riser, S. C., Russell, J. L., Talley, L. D., ... & Sarmiento, J. L. (2018). Autonomous Biogeochemical Floats Detect Significant Carbon Dioxide Outgassing in the High- Latitude Southern Ocean. *Geophysical Research Letters,* 45(17), 9049-9057.

21. Guay, C. K., & Bishop, J. K. (2002). A rapid birefringence method for measuring suspended CaCO3 concentrations in seawater. *Deep Sea Research Part I: Oceanographic Research Papers*, *49*(1), 197-210.

22. Halsey, K. H., & Jones, B. M. (2015). Phytoplankton strategies for photosynthetic energy allocation. *Annual review of marine science*, *7*, 265-297.

23. Huber, P. J. (1981). Robust Statistics. Hoboken, NJ: John Wiley & Sons, Inc.

24. Martínez-Vicente, V., Evers-King, H., Roy, S., Kostadinov, T. S., Tarran, G. A., Graff, J. R., ... & Röttgers, R. (2017). Intercomparison of ocean color algorithms for picophytoplankton carbon in the ocean. *Frontiers in Marine Science*, *4*, 378.

25. MATLAB and Statistics Toolbox, The MathWorks, Inc., Natick, Massachusetts, United States.

26. Mignot, A., Claustre, H., Uitz, J., Poteau, A., D'Ortenzio, F., & Xing, X. (2014). Understanding the seasonal dynamics of phytoplankton biomass and the deep chlorophyll maximum in oligotrophic environments: A Bio-Argo float investigation. *Global Biogeochemical Cycles*, 28(8), 856-876.

27. Mignot, A., Ferrari, R., & Claustre, H. (2018). Floats with bio-optical sensors reveal what processes trigger the North Atlantic bloom. *Nature communications*, 9(1), 190.

28. Moré, J. J., & Sorensen, D. C. (1983). Computing a trust region step. *SIAM Journal on Scientific and Statistical Computing*, 4(3), 553-572.

29. Morel, A. (1988). Optical modeling of the upper ocean in relation to its biogenous matter content (case I waters). Journal of geophysical research: oceans, 93(C9), 10749-10768.

30. Morel, A., & Ahn, Y. H. (1990). Optical efficiency factors of free-living marine bacteria: Influence of bacterioplankton upon the optical properties and particulate organic carbon in oceanic waters. *Journal of Marine Research*, *48*(1), 145-175.

31. Morel, A., & Ahn, Y. H. (1991). Optics of heterotrophic nanoflagellates and ciliates: A tentative assessment of their scattering role in oceanic waters compared to those of bacterial and algal cells. *Journal of Marine Research*, *49*(1), 177-202.

32. Morel, A., & Maritorena, S. (2001). Bio-optical properties of oceanic waters: A reappraisal. *Journal of Geophysical Research: Oceans*, *106*(C4), 7163-7180.

33. Organelli, E., Barbieux, M., Claustre, H., Schmechtig, C., Poteau, A., Bricaud, A., ... & Leymarie, E. (2017). Two databases derived from BGC-Argo float measurements for marine biogeochemical and bio-optical applications. *Earth System Science Data*, *9*, 861-880.

34. Organelli, E., Dall'Olmo, G., Brewin, R. J., Tarran, G. A., Boss, E., & Bricaud, A. (2018). The open-ocean missing backscattering is in the structural complexity of particles. *Nature Communications*, *9*(1), 5439.

35. Poteau, A., Boss, E., & Claustre, H. (2017). Particulate concentration and seasonal dynamics in the mesopelagic ocean based on the backscattering coefficient measured with Biogeochemical- Argo floats. *Geophysical Research Letters*, 44(13), 6933-6939.

36. Siegel, D. A., Behrenfeld, M. J., Maritorena, S., McClain, C. R., Antoine, D., Bailey, S. W., ... & Eplee Jr, R. E. (2013). Regional to global assessments of phytoplankton dynamics from the SeaWiFS mission. *Remote Sensing of Environment*, *135*, 77-91.

37. Siokou-Frangou, I., Christaki, U., Mazzocchi, M. G., Montresor, M., Ribera d'Alcalà, M., Vaqué, D., & Zingone, A. (2010). Plankton in the open Mediterranean Sea: a review.

38. Sosik. H. M. Characterizing seawater constituents from optical properties. In M. Babin, C. S. Roesler and J. J. Cullen [eds.]. Real-time coastal observing systems for ecosystem dynamics and harmful algal blooms. UNESCO, pp. 281-329. (peer reviewed) (2008).

39. Stramski, D., & Kiefer, D. A. (1991). Light scattering by microorganisms in the open ocean. *Progress in Oceanography*, *28*(4), 343-383.

40. Stramski, D., Boss, E., Bogucki, D., & Voss, K. J. (2004). The role of seawater constituents in light backscattering in the ocean. *Progress in Oceanography*, *61*(1), 27-56.

41. Twardowski, M., Zhang, X., Vagle, S., Sullivan, J., Freeman, S., Czerski, H., ... & Kattawar, G. (2012). The optical volume scattering function in a surf zone inverted to derive sediment and bubble particle subpopulations. *Journal of Geophysical Research: Oceans*, *117*(C7).

42. Uitz, J., Claustre, H., Griffiths, F. B., Ras, J., Garcia, N., & Sandroni, V. (2009). A phytoplankton class-specific primary production model applied to the Kerguelen Islands region (Southern Ocean). *Deep Sea Research Part I: Oceanographic Research Papers*, *56*(4), 541-560.

43. Volpe, G., Santoleri, R., Vellucci, V., d'Alcalà, M. R., Marullo, S., & d'Ortenzio, F. (2007). The colour of the Mediterranean Sea: Global versus regional bio-optical algorithms evaluation and implication for satellite chlorophyll estimates. *Remote Sensing of Environment*, *107*(4), 625-638.

44. Westberry, T., Behrenfeld, M. J., Siegel, D. A., & Boss, E. (2008). Carbon-based primary productivity modeling with vertically resolved photoacclimation. *Global Biogeochemical Cycles*, 22(2).

45. Westberry, T. K., Dall'Olmo, G., Boss, E., Behrenfeld, M. J., & Moutin, T. (2010). Coherence of particulate beam attenuation and backscattering coefficients in diverse open ocean environments. *Optics Express*, *18*(15), 15419-15425.

46. Westberry, T. K., Schultz, P., Behrenfeld, M. J., Dunne, J. P., Hiscock, M. R., Maritorena, S., ... & Siegel, D. A. (2016). Annual cycles of phytoplankton biomass in the subarctic Atlantic and Pacific Ocean. *Global Biogeochemical Cycles*, 30(2), 175-190.
47. Zhang, X., Lewis, M., & Johnson, B. (1998). Influence of bubbles on scattering of light in the ocean. *Applied Optics*, *37*(27), 6525-6536.
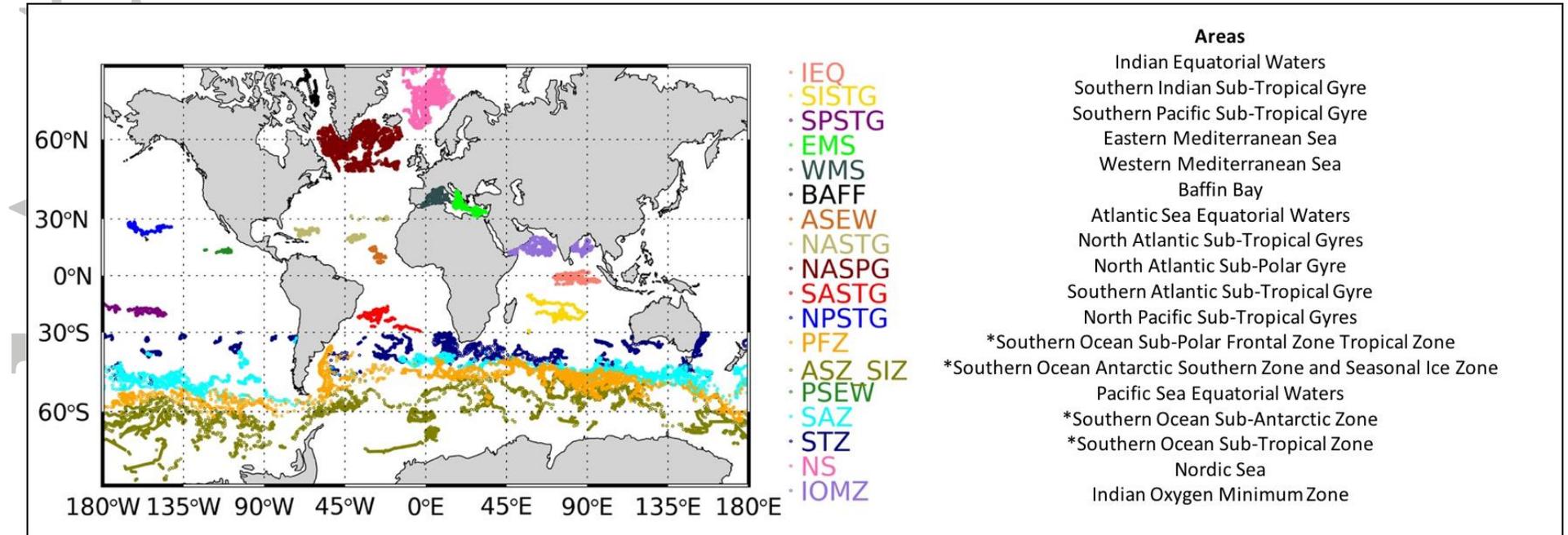
Figure 1: Geographical distribution of the BGC-Argo dataset on a global ocean scale. Each colour represents sampling areas and abbreviations. * indicates data acquired in four regions below 30°S which have been delineated by using temperature profiles (Gray et al., 2018): Sub-Tropical Zone (STZ) with a temperature at 100 m above 11°C; the Sub-Antarctic Zone (SAZ) with a temperature at 400 m below 5°C; the Polar Frontal Zone (PFZ) with the minimum temperature between 0 and 200 m above 2°C; the Antarctic Southern Zone and Seasonal Ice Zone (ASZ_SIZ) minimum temperature between 0 and 200 m below 2°C.
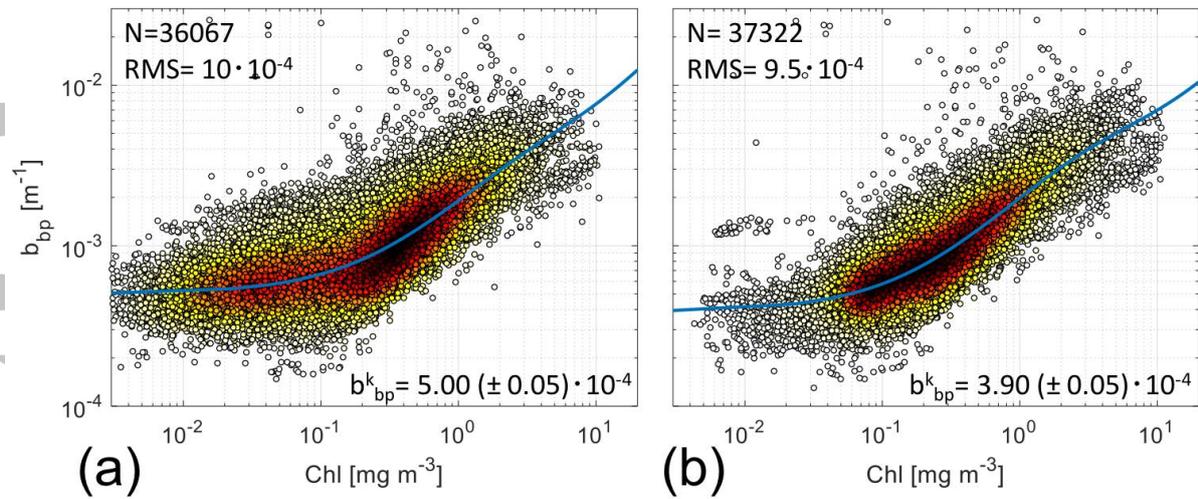
Figure 2: Plot density between Chl and b_{bp} (700) within the surface layer (panel a) and the euphotic layer (panel b). Both panels include the number of observations (*N*) and the RMS (in m^{-1}). The b_{bp}^{k} estimation (in m^{-1}) with two standard deviation as confidence limit ($\pm 2\sigma$) is also reported. Chl values < 0.01 mg m^{-3} are not included in the fit computations. The plots are presented in logarithmic scale in both axes though the fit has been calculated in linear scale. Dot density is indicated as color from white (low density) to black (high density).
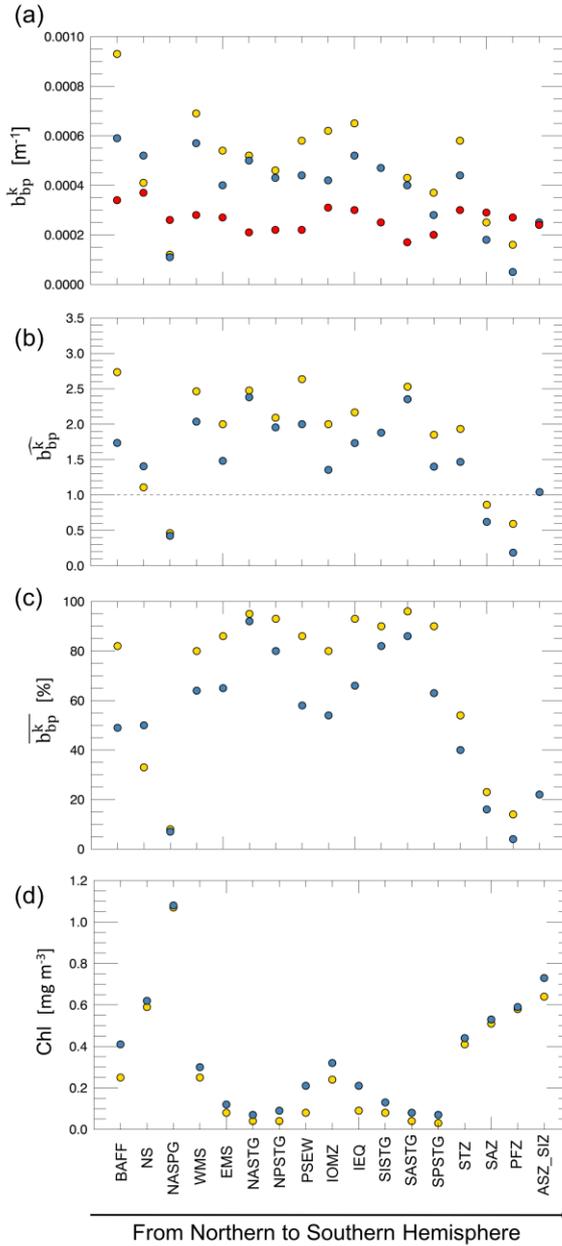
Figure 3: Geographical distribution of b_{bp}^k (in m^{-1}) in the three layers: surface (gold), euphotic (blue) and bottom (red) (a). The $\widehat{b_{bp}^k}$ for the surface (gold) and euphotic (blue) layers for each area (b). The dashed line indicates the case where $\widehat{b_{bp}^k}$ estimates between surface or euphotic layer with bottom layer are close to the same value. Panel c shows the $\overline{b_{bp}^k}$ (in %) for each area and layer (gold for surface layer; blue for euphotic layer). The model performance, in terms of RMS (m^{-1}) and interval of confidence at 95% for each b_{bp}^k estimation is reported in the supplementary information (see Figures S3, S4; Table S2). ASEW area is not included in this analysis due to the low performance of the model and highest uncertainties in b_{bp}^k assessment in both layer (for details see the supplementary materials). Note that the areas have been sorted from the northern to the southern hemisphere. Panel d shows the mean Chl values for each region and layers (gold for surface layer and blue for euphotic layer). See Table 1 for locations and abbreviations.
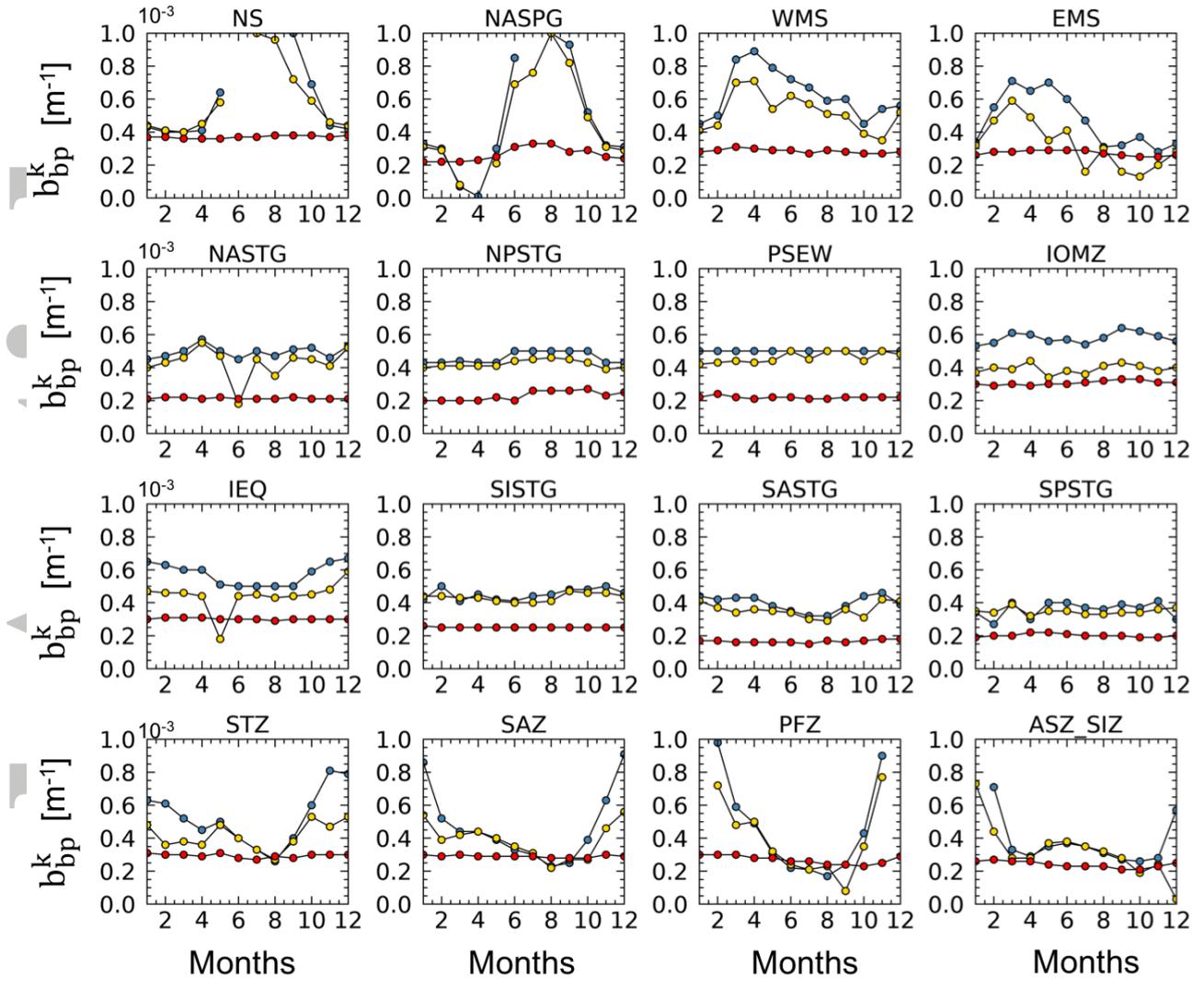
Figure 4: Temporal variability of b_{bp}^k (in m^{-1}) for each area and all the three layers: surface (gold), euphotic (blue) and bottom (red). The model performance, in terms of RMS (m^{-1}) and interval of confidence at 95% for each monthly b_{bp}^k estimation, are reported in the supplementary materials (see Tables S3, S4 and S5). ASEW and BAFF areas are not included in the analysis due to the absence/limited number of observations that prevents the description of the annual cycle. See Table 1 for locations and abbreviations.